Angle-domain common-image gathers for migration velocity analysis by wavefield-continuation imaging

Biondo Biondi[1] and William W. Symes[2]

ABSTRACT

We analyze the kinematic properties of offset-domain common image gathers (CIGs) and angle-domain CIGs (ADCIGs) computed by wavefield-continuation migration. Our results are valid regardless of whether the CIGs were obtained by using the correct migration velocity. They thus can be used as a theoretical basis for developing migration velocity analysis (MVA) methods that exploit the velocity information contained in ADCIGs.

We demonstrate that in an ADCIG cube, the image point lies on the normal to the apparent reflector dip that passes through the point where the source ray intersects the receiver ray. The image-point position on the normal depends on the velocity error; when the velocity is correct, the image point coincides with the point where the source ray intersects the receiver ray. Starting from this geometric result, we derive an analytical expression for the expected movements of the image points in ADCIGs as functions of the traveltime perturbation caused by velocity errors. By applying this analytical result and assuming stationary raypaths (i.e., small velocity errors), we then derive two expressions for the residual moveout (RMO) function in ADCIGs. We verify our theoretical results and test the accuracy of the proposed RMO functions by analyzing the migration results of a synthetic data set with a wide range of reflector dips.

Our kinematic analysis leads also to the development of a new method for computing ADCIGs when significant geological dips cause strong artifacts in the AD-CIGs computed by conventional methods. The proposed method is based on the computation of offset-domain CIGs along the vertical-offset axis and on the "optimal" combination of these new CIGs with conventional CIGs. We demonstrate the need for and the advantages of the proposed method on a real data set acquired in the North Sea.

INTRODUCTION

With wavefield-continuation migration methods being used routinely for imaging projects in complex areas, the ability to perform migration velocity analysis (MVA) starting from the results of wavefield-continuation migration is becoming essential to advanced seismic imaging. As for Kirchhoff imaging, MVA for wavefield-continuation imaging is mostly based on the information provided by the analysis of common image gather (CIGs). For wavefield-continuation methods, most of the current MVA methods start from angle-domain CIGs (ADCIGs) (Biondi and Sava, 1999; Clapp and Biondi, 2000; Liu et al., 2001; Mosher et al., 2001), though the use of more conventional surface-offset-domain CIGs is also being evaluated (Stork et al., 2002).

Both kinematic and amplitude properties (de Bruin et al., 1990; Wapenaar et al., 1999; Sava et al., 2001; de Hoop et al., 2004) have been analyzed in the literature for ADCIGs obtained when the migration velocity is accurate. On the contrary, the properties of the ADCIGs obtained when the migration velocity is inaccurate have been only qualitatively discussed in the literature. This lack of quantitative understanding may lead to errors when performing MVA from ADCIGs. In this paper, we analyze the kinematic properties of ADCIGs under general conditions (accurate or inaccurate velocity). If the migration velocity is inaccurate, our analysis requires only a smooth migration velocity function in the neighborhood of the imaging point. We discuss this condition more extensively in the first section. The application of the insights provided by our analysis may substantially improve the results of the following three procedures: (1) measurement of velocity errors from ADCIGs by residual moveout (RMO) analysis, (2) inversion of RMO measurements into velocity updates, and (3) computation of ADCIGs in the presence of complex geologic structure.

Our analysis demonstrates that in an image cube transformed to the angle domain (in the following we refer to this image cube as an ADCIG cube), the image point lies on the normal to the apparent reflector dip passing through the point

where the source ray intersects the receiver ray. We exploit this result to define an analytical expression for the expected movements of the image points in ADCIGs as a function of the traveltime perturbation caused by velocity errors. This leads us to the definition of two alternative residual moveout functions that can be applied when measuring velocity errors from migrated images. We test the accuracy of these alternatives, and discuss their relative advantages and disadvantages. Furthermore, the availability of a quantitative expression for the expected movements of the image points is crucial when inverting those movements into velocity corrections by either simple vertical updating or sophisticated tomographic methods. Therefore, our results ought to be incorporated in velocity updating methods.

Our theoretical result also implies that ADCIGs are immune, at least to first order in velocity perturbations, from the distortions caused by *image-point dispersal*. Image-point dispersal occurs when migration velocity errors cause events from the same segment of a dipping reflector to be imaged at different locations (Etgen, 1990). This inconsistency creates substantial problems when using dipping reflections for velocity updating; its absence makes ADCIGs even more attractive for MVA.

The computation of ADCIGs is based on a decomposition (usually performed by slant stacks) of the wavefield either before imaging (de Bruin et al., 1990; Mosher et al., 1997; Prucha et al., 1999; Xie and Wu, 2002), or after imaging (Biondi and Shan, 2002; Rickett and Sava, 2002; Sava and Fomel, 2003). In either case, the slant-stack transformation is usually applied along the horizontal subsurface-offset axis. However, when the geologic dips are steep, this "conventional" way of computing CIGs does not produce useful gathers, even if it is kinematically valid for geologic dips less than $90°$. As the geologic dips increase, the horizontal-offset CIGs (HOCIGs) degenerate, and their focusing around zero offset blurs. This limitation of HOCIGs can be sidestepped by computing offset-domain CIGs along the vertical subsurface-offset axis (VOCIGs) (Biondi and Shan, 2002). Although neither set of offset-domain gathers (HOCIG or VOCIG) provides useful information for the whole range of geologic dips, an appropriate combination of the two sets does. Our analysis of the kinematic properties of ADCIGs suggests a simple and effective method for combining a HOCIG cube with a VOCIG cube to create an ADCIG cube that is immune to artifacts in the presence of arbitrary geologic dips.

We present and demonstrate the main results of this paper using a ray-theoretical approach, though we apply the theory to analyze ADCIGs obtained by wavefield-continuation method. Our approach is apparently inconsistent, but it is motivated by the fact that the ray-based analysis is more intuitive than the equivalent wave-based analysis. The two approaches are obviously connected through the plane-wave decomposition performed by slant stacking. We equate the propagation direction of plane waves with the propagation direction of specular rays; thus, we implicitly make a stationary-phase approximation that assumes that the seismic events are not dispersive (i.e., that wavefronts are locally planar and coherent for all frequencies). This assumption is not strictly necessary because our analysis is valid for each frequency component, but nonetheless we believe that the advantages in simplicity are worthwhile despite the apparent loss of generality.

Our ray-based analysis of ADCIGs is also founded on the concept of *subsurface offset*. The physical interpretation of the subsurface offset is immediate when source-receiver migration is used. In this case, the subsurface offset coincides with the data offset after datuming by survey sinking. For shot-profile migration, the equivalence between data offsets at depth and subsurface offsets is demonstrated by Wapenaar and Berkhout (1987) and Biondi (2003). De Bruin (1992) presents an alternative wave-theoretical analysis of ADCIGs obtained by shot-profile migration using wavefield continuation when the migration velocity is correct.

ADCIGs have been introduced also for Kirchhoff migration (Xu et al., 2001; Brandsberg-Dahl et al., 2003), and they can be used for MVA with Kirchhoff methods as well (Brandsberg-Dahl et al., 1999). We believe that the analysis presented in this paper might be extended to ADCIGs computed by Kirchhoff migration. However, in complex media, the two types of ADCIG have subtle kinematic differences, as clearly demonstrated by Stolk and Symes (2004). Therefore, the application of our results to Kirchhoff ADCIGs may require further analysis that is beyond the scope of this paper.

We start our paper by briefly reviewing the methodology for computing offset-domain and angle-domain CIGs by wavefield-continuation migration. The second section analyzes the kinematic properties of CIGs and ADCIGs, and contains the main theoretical development of the paper. The third section exploits the theoretical results to define a robust algorithm to compute ADCIGs in the presence of geological structure, and illustrates its advantages with a real-data example. The fourth section verifies the theoretical analysis by using it to predict reflector movements in the migrated images of a synthetic data set. Finally, the fifth section derives two expressions for the RMO function to be applied for measuring velocity errors from migrated images.

COMPUTATION OF COMMON IMAGE GATHERS BY WAVEFIELD CONTINUATION

In this section we briefly revisit the method for computing (CIGs) by wavefield-continuation migration. The following development assumes that both the source wavefield and the receiver wavefield have been numerically propagated into the subsurface. The analytical expressions represent wavefields in the time domain; thus, they appear to implicitly assume that the wavefields have been propagated in the time domain. However, all the considerations and results that follow are independent of the specific numerical method that was used for propagating the wavefields. They are obviously valid for reverse-time migration when the wavefields are propagated in the time domain (Baysal et al., 1983; Whitmore, 1983; Etgen, 1986; Biondi and Shan, 2002). They are also valid when the wavefields are propagated by downward continuation in the frequency domain, if there are no overturned events. Furthermore, our results are valid when source-receiver migration is used instead of shot-profile migration; the physical interpretation of the concepts of subsurface offset and of the imaging point in the subsurface-offset domain is actually more immediate for source-receiver migration than for shot-profile migration.

The conventional imaging condition for shot-profile migration is based on the crosscorrelation in time of the source wavefield (S) with the receiver wavefield (R). The equivalent of the

stacked image is the average over sources (s) of the zero lag of this crosscorrelation; that is,

$$I(z, x) = \sum_s \sum_t S_s(t, z, x) R_s(t, z, x), \qquad (1)$$

where z and x are respectively depth and the horizontal axes, and t is time. The result of this imaging condition is equivalent to stacking over offsets with Kirchhoff migration.

The imaging condition expressed in equation (1) has the substantial disadvantage of not providing prestack information that can be used for either velocity updates or amplitude analysis. Equation 1 can be generalized (Biondi and Shan,2002; Rickett and Sava, 2002) by crosscorrelating the wavefields shifted horizontally with respect to each other. The prestack image becomes a function of the horizontal relative shift, which has the physical meaning of a *subsurface half offset* (x_h). It can be computed as

$$I(z, x, x_h) = \sum_s \sum_t S_s(t, z, x - x_h) R_s(t, z, x + x_h). \quad (2)$$

A section of the image cube $I(z, x, x_h)$ taken at constant horizontal location x is a horizontal offset common image gather (HOCIG). The whole image cube can be seen as a collection of HOCIGs. Sava and Fomel (2003) presented a simple method for transforming HOCIGs into ADCIGs by a slant-stack transformation (Schultz and Claerbout, 1978) applied independently to each HOCIG:

$$I_{\gamma_x}(z, x, \gamma) = \text{SlantStack}[I(z, x, x_h)]; \qquad (3)$$

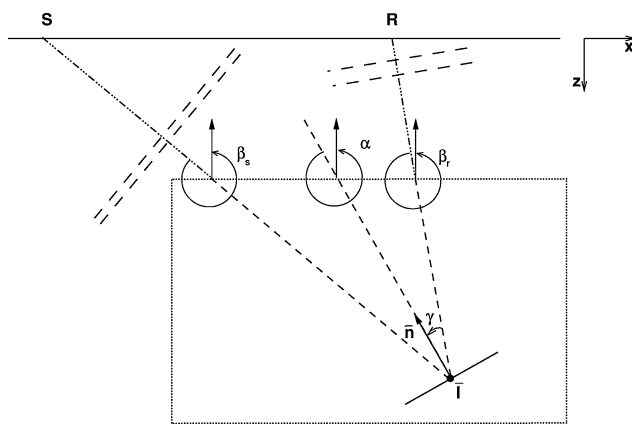where γ is the aperture angle of the reflection, as shown in Figure 1.

Figure 1. Geometry of an ADCIG for a single event migrated with the wrong (low in this case) velocity. Depending on the context, the angles can be either the angles formed by the propagation direction of the rays, or by the propagation direction of the associated plane waves. The propagation direction of the source ray forms the angle β_s with the vertical, and the propagation direction of the receiver ray forms the angle β_r with the vertical; γ is the apparent aperture angle, and α is the apparent reflector dip. The source ray and the receiver ray cross at $\bar{\mathbf{I}}$. The arrows indicate positive angles; that is, in the figure, β_s, β_r, and α are negative (larger than π) and γ is positive. This sign convention is consistent with upward propagating rays (waves).

This transformation from HOCIG to ADCIG is based on the following relationship between the aperture angle and the slope ($\partial z/\partial x_h$) measured in image space:

$$-\frac{\partial z}{\partial x_h}\bigg|_{t,x} = \tan \gamma = -\frac{k_{x_h}}{k_z}, \qquad (4)$$

where k_{x_h} and k_z are respectively the half-offset wavenumber and the vertical wavenumber. The relationship between $\tan \gamma$ and the wavenumbers suggests that the transformation to ADCIGs can be accomplished in the Fourier domain by a simple radial-trace transform (Sava and Fomel, 2003).

Equation 4 relates slopes in the wavenumber domain to ray-propagation directions in the time domain; it is based on an implicit stationary-phase assumption, as we discussed in the previous section. In other words, we identify the direction of the phase-velocity vector of a plane wave with the direction of propagation of the ray normal to the plane wave. This identification of plane waves with rays is necessary only locally around the imaging point, as it is graphically represented by the box around the imaging point in Figure 1.

Sava and Fomel (2003) demonstrated the validity of equation 4 based only on Snell's law and on the geometric relationships between the propagation directions of the source ray (determined by β_s in Figure 1) and receiver ray (determined by β_r in Figure 1). Its validity is thus independent of the focusing of the reflected energy at zero offset; that is, it is valid regardless of whether the image point coincides with the intersection of the two rays (marked as $\bar{\mathbf{I}}$ in Figure 1). In other words, it is independent of whether the correct migration velocity is used. The only assumption about the migration velocity is that the velocity at the imaging depth is the same along the source ray and the receiver ray. This condition is obviously fulfilled when the reflected energy focuses at zero offset, but it is, at least approximately, fulfilled in most practical situations of interest. In most practical cases, we can assume that the migration velocity function is smooth in a neighborhood of the imaging point. The extent of this neighborhood depends on the velocity error because it depends on the distance between the end point of the source ray and the end point of the receiver ray (see Figure 2). The only exception of practical importance is when the reflection is caused by a high-contrast interface, such as a salt-sediment interface. In these cases, our results must be applied with particular care. When the migration velocity is correct, α and γ are respectively the true reflector dip and the true aperture angle; otherwise they are the *apparent* reflector dip and the apparent aperture angle. In Figure 1, the box around the imaging point signifies the local nature of the geometric relationships relevant to our discussion; it emphasizes that these relationships depend only on the local velocity function.

When the velocity is correct, the image point obviously coincides with the crossing point of the two rays $\bar{\mathbf{I}}$. However, the position of the image point when the velocity is not correct has been left undefined by previous analyses (Prucha et al., 1999; Sava and Fomel, 2003). In this paper, we demonstrate the important result that in an ADCIG, when the migration velocity is incorrect, the image point lies along the direction normal to the apparent geological dip. We identify this normal direction with the unit vector $\mathbf{n}$ that we define as oriented in the direction of decreasing traveltimes for the rays (see Figure 1). Stork (1992)

and Meng and Bleistein (2001) postulate a similar behavior for the CIGs obtained by common-offset Kirchhoff migration.

Notice that the geometric arguments presented in this paper are based on the assumption that the source and receiver rays cross even when the data were migrated with the wrong velocity (below the imaging point in case of too low migration velocity and above the imaging point in the opposite case). This assumption is valid in two dimensions except in degenerate cases of marginal practical interest (e.g. diverging rays). In three dimensions, this assumption is more easily violated because two rays are not always coplanar. In contrast with the 2D case, in three dimensions the plane-wave interpretation of AD-CIGs would actually simplify the analysis with respect to the ray interpretation because plane waves always intersect even when the migration velocity is wrong. We consider the generalization to three dimensions of our 2D results beyond the scope of this paper, though this generalization is possible once 3D ADCIGs are defined (de Bruin, 1992; Biondi et al., 2003).

As will be discussed in the following section and illustrated later by the real-data example in Figure 4a, the HOCIGs, and consequently the ADCIGs computed from the HOCIGs (Figure 5a), have problems when the reflectors are steeply dipping. At the limit, the HOCIGs become useless when imaging nearly vertical reflectors using either overturned events or prismatic reflections. To create useful ADCIGs in these situations, Biondi and Shan (2002) introduced a new kind of CIG. This new kind of CIG is computed by introducing a *vertical half offset* (z_h) into equation 1 to obtain

$$I(z, x, z_h) = \sum_s \sum_t S_s(t, z - z_h, x) R_s(t, z + z_h, x). \quad (5)$$

A section of the image cube computed by equation 5 taken at constant depth z is a vertical offset common image gather (VOCIG).

As for the HOCIGs, the VOCIGs can be transformed into an ADCIG by applying a slant-stack transformation to each

individual VOCIG; that is,

$$I_{\gamma_z}(z, x, \gamma) = \text{SlantStack}[I(z, x, z_h)]. \quad (6)$$

This transformation is based on the following relationship between the aperture angle and the slope $\partial x/\partial z_h$ measured in image space:

$$\left.\frac{\partial x}{\partial z_h}\right|_{t,z} = \tan \gamma = \frac{k_{z_h}}{k_x}. \quad (7)$$

Equation 7 is analogous to equation 4, and its validity can be trivially demonstrated from equation 4 by a simple axes rotation. However, notice the sign differences between equation 7 and equation 4 caused by the conventions defined in Figure 1.

Notice that our notation distinguishes the result of the two transformations to ADCIG (I_{γ_x} and I_{γ_z}) because they are different objects even though they are images defined in the same domain (z, x, γ). One of the main results of this paper is the definition of the relationship between I_{γ_x} and I_{γ_z}, and the derivation of a robust algorithm to "optimally" merge the two sets of ADCIGs. To achieve this goal, we first analyze the kinematic properties of HOCIGs and VOCIGs.

KINEMATIC PROPERTIES OF COMMON IMAGE GATHERS

To analyze the kinematic properties of HOCIGs and VO-CIGs, it is useful to observe that they are just particular cases of offset-domain gathers. In general, the offset can be oriented along any arbitrary direction. In particular, the offset direction aligned with the apparent geological dip of the imaged event has unique properties. We will refer to this offset as the *geological-dip offset*, and the corresponding CIGs as geological offset CIGs (GOCIGs).

Figure 2 illustrates the geometry of the different kinds of offset-domain CIGs for a single event. In this sketch, the migration velocity is assumed to be lower than the true velocity, and thus the reflections are imaged too shallow and above the point where the actual source ray crosses the actual receiver ray ($\bar{\mathbf{I}}$). When HOCIGs are computed, the end point of the source ray ($\mathbf{S}_{x_h}$) and the end point of the receiver ray ($\mathbf{R}_{x_h}$) are at the same depth. By definition, the imaging point $\mathbf{I}_{x_h}$ is midway between $\mathbf{S}_{x_h}$ and $\mathbf{R}_{x_h}$, and the imaging half offset is $x_h = (\mathbf{R}_{x_h} - \mathbf{I}_{x_h}) \cdot \mathbf{x}$. Similarly, when VOCIGs are computed, the end point of the source ray ($\mathbf{S}_{z_h}$) and the end point of the receiver ray ($\mathbf{R}_{z_h}$) are at the same horizontal location. The imaging point $\mathbf{I}_{z_h}$ is midway between $\mathbf{S}_{z_h}$ and $\mathbf{R}_{z_h}$, and the imaging half offset is $z_h = (\mathbf{R}_{z_h} - \mathbf{I}_{z_h}) \cdot \mathbf{z}$. When the offset direction is oriented along the apparent geological dip α (what we called the geological-dip offset direction), the end point of the source ray is $\mathbf{S}_0$ and the end point of the receiver ray is $\mathbf{R}_0$. The imaging point $\mathbf{I}_0$ is midway between $\mathbf{S}_0$ and $\mathbf{R}_0$, and the imaging half offset is $\mathbf{h}_0 = \mathbf{R}_0 - \mathbf{I}_0$. Notice that we define the geological-dip half offset $\mathbf{h}_0$ as a vector because it can be oriented arbitrarily with respect to the coordinate axes.

Figure 2 shows that both $\mathbf{I}_{x_h}$ and $\mathbf{I}_{z_h}$ lie on the line passing through $\mathbf{S}_0$, $\mathbf{I}_0$, and $\mathbf{R}_0$. This is an important property of the offset-domain CIGs and is based on a crucial constraint imposed on our geometric construction; that is, the traveltime along the source ray summed with the traveltime along the receiver ray is the same for all the offset directions, and is equal to
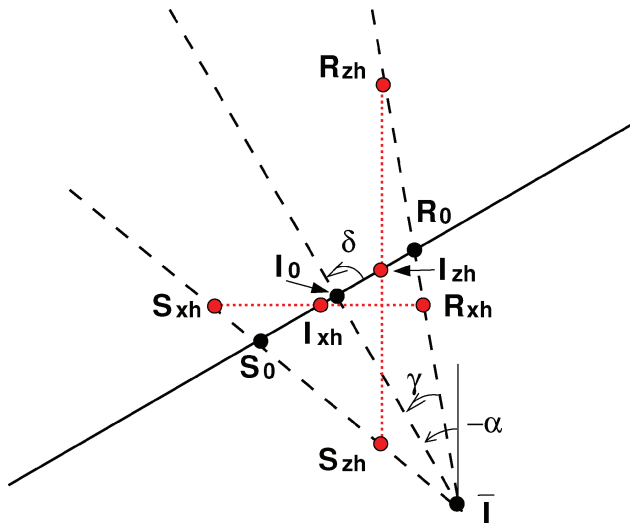

Figure 2. Geometry of the three different kinds of offset-domain (horizontal, vertical, and geological-dip) CIG for a single event migrated with the wrong velocity. $\mathbf{I}_{x_h}$ is the horizontal-offset image point, $\mathbf{I}_{z_h}$ is the vertical-offset image point, and $\mathbf{I}_0$ is the geological-dip offset image point.

the recording time of the event. The independence of the total traveltimes from the offset directions is a direct consequence of taking the zero lag of the crosscorrelation in the imaging conditions of equations 2 and 5. This constraint, together with the assumption of locally constant velocity discussed above, directly leads to the following equalities:

$$\left|\mathbf{S_{x_h}} - \mathbf{S_0}\right| = \left|\mathbf{R_{x_h}} - \mathbf{R_0}\right|, \quad \text{and} \quad \left|\mathbf{S_{z_h}} - \mathbf{S_0}\right| = \left|\mathbf{R_{z_h}} - \mathbf{R_0}\right|, \quad (8)$$

which in turn are at the basis of the collinearity of $\mathbf{I_0}$, $\mathbf{I_{x_h}}$, and $\mathbf{I_{z_h}}$.

The offsets along the different directions are linked by the following simple relationship, which can be readily derived by trigonometry applied to Figure 2:

$$x_h = \frac{\widetilde{h_0}}{\cos \alpha}, \quad (9)$$

$$z_h = \frac{\widetilde{h_0}}{\sin \alpha}, \quad (10)$$

where $\widetilde{h_0} = |\mathbf{h}_0| \, \text{sign} \, (\sin \delta)$, with δ being the angle formed by $\mathbf{h}_0$ with the normal $\mathbf{n}$ (see Figure 2). Notice that the definition of $\widetilde{h_0}$ is such that its sign depends on whether $\mathbf{I_0}$ is before or beyond $\mathbf{\bar{I}}$.

Although $\mathbf{I_{x_h}}$ and $\mathbf{I_{z_h}}$ are both collinear with $\mathbf{I_0}$, they are shifted with respect to each other and with respect to $\mathbf{I_0}$. The shifts of the imaging points $\mathbf{I_{x_h}}$ and $\mathbf{I_{z_h}}$ with respect to $\mathbf{I_0}$ can be easily expressed in terms of the offset $\mathbf{h}_0$ and the angles α and γ as follows:

$$\Delta \mathbf{I}_{x_h} = (\mathbf{I_{x_h}} - \mathbf{I_0}) = \mathbf{h}_0 \tan \gamma \tan \alpha, \quad (11)$$

$$\Delta \mathbf{I}_{z_h} = (\mathbf{I_{z_h}} - \mathbf{I_0}) = -\mathbf{h}_0 \frac{\tan \gamma}{\tan \alpha}. \quad (12)$$

The two imaging points $\mathbf{I_{x_h}}$ and $\mathbf{I_{z_h}}$ are always on the opposite side of $\mathbf{I_0}$; their distance prevents us from constructively averaging HOCIGs with VOCIGs to create a single set of offset-domain CIGs.

Notice the dependence of $\Delta \mathbf{I}_{x_h}$ and $\Delta \mathbf{I}_{z_h}$ on the aperture angle γ and the geological dip α. The dependence on γ causes events with different aperture angles to be imaged at different locations, even if they originated at the same reflecting point in the subsurface. This phenomenon is related to the well known *reflector-point dispersal* in common midpoint gathers. In this context, this dispersal is a consequence of using a wrong imaging velocity, and we will refer to it as *image-point dispersal*. We now discuss how the transformation to ADCIGs overcomes the problems related to the image-point shift and thus removes, at least to first order, the image-point dispersal.

Kinematic properties of ADCIGs

The transformation to the angle domain, as defined by equations 3 and 4 for HOCIGs, and equations 6 and 7 for VOCIGs, acts on each offset-domain CIG independently. Therefore, when the reflected energy does not focus at zero offset, the transformation to the angle domain shifts the image point along the direction orthogonal to the offset to reach the image point in the angle domain $\mathbf{I}_\gamma$. The horizontal-offset image point ($\mathbf{I_{x_h}}$) shifts vertically, and the vertical-offset image point ($\mathbf{I_{z_h}}$) shifts horizontally. We will demonstrate the two following important properties of this *normal shift*:

1) The normal shift corrects for the effects of the offset direction on the location of the image point; that is, the transformation to the angle domain shifts the image points from different locations in the offset domain ($\mathbf{I_{x_h}}$, $\mathbf{I_{z_h}}$, and $\mathbf{I_0}$) to the same location in the angle domain ($\mathbf{I}_\gamma$).

2) The image location in the angle domain ($\mathbf{I}_\gamma$) lies on the normal to the apparent geological dip passing through the crossing point of the source and receiver rays ($\mathbf{\bar{I}}$). $\mathbf{I}_\gamma$ is located at the crossing point of the lines passing through $\mathbf{S_0}$ and $\mathbf{R_0}$ and orthogonal to the source ray and receiver ray, respectively. The shift along the normal to the reflector, caused by the transformation to angle domain, is thus equal to

$$\Delta \mathbf{n}_\gamma = (\mathbf{I}_\gamma - \mathbf{I_0}) = \widetilde{h_0} \tan \gamma \, \mathbf{n} = \tan^2 \gamma \, \Delta \mathbf{n}_{h_0}, \quad (13)$$

where $\Delta \mathbf{n}_{h_0} = (\widetilde{h_0}/\tan \gamma) \, \mathbf{n}$ is the normal shift in the geological-dip domain. The total normal shift caused by incomplete focusing at zero offset is thus equal to

$$\Delta \mathbf{n}_{\text{tot}} = (\mathbf{I}_\gamma - \mathbf{\bar{I}}) = \Delta \mathbf{n}_{h_0} + \Delta \mathbf{n}_\gamma$$

$$= \Delta \mathbf{n}_{h_0}(1 + \tan^2 \gamma) = \frac{\Delta \mathbf{n}_{h_0}}{\cos^2 \gamma}. \quad (14)$$

Figure 3 illustrates properties (1) and (2). These properties have several important consequences. The three results most relevant to migration velocity analysis are

1) ADCIGs obtained from HOCIGs and VOCIGs can be constructively averaged, in contrast to the original HOCIGs and VOCIGs. We exploit this property to introduce a robust algorithm for creating a single set of ADCIGs that is insensitive to geological dips and thus is ready to be analyzed for velocity information.

2) The reflector-point dispersal that negatively affects offset-domain CIGs is corrected in the ADCIGs, at least to first order. If we assume the raypaths to be stationary (i.e., small
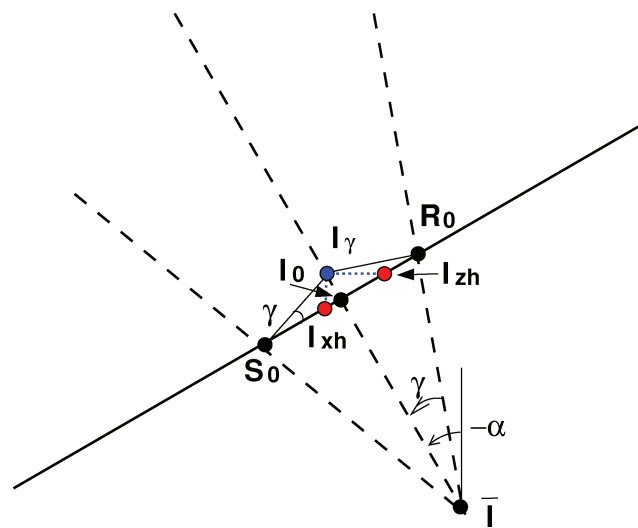

Figure 3. Geometry of an ADCIG for a single event migrated with the wrong velocity. The transformation to the angle domain shifts all the offset-domain image points ($\mathbf{I_{x_h}}$, $\mathbf{I_{z_h}}$, $\mathbf{I_0}$) to the same angle-domain image point $\mathbf{I}_\gamma$.

velocity error), for a given reflecting segment the image points for all aperture angles γ share the same apparent dip, and thus they are all aligned along the normal to the apparent reflector dip.

3) From equation 14, invoking Fermat's principle and applying simple trigonometry, we can also easily derive a relationship between the total normal shift $\Delta \mathbf{n}_{\mathrm{tot}}$ and the total traveltime perturbation caused by velocity errors as follows (Etgen, 1990; Stork, 1992):

$$\Delta \mathbf{n}_{\mathrm{tot}} = \frac{\Delta t}{2S \cos \gamma} \mathbf{n}, \qquad (15)$$

where S is the background slowness around the image point, and Δt is defined as the difference between the perturbed traveltime and the background traveltime. We will exploit this relationship to introduce a simple and accurate expression for measuring residual moveouts from ADCIGs.

Demonstration of kinematic properties of ADCIGs

Properties (1) and (2) can be demonstrated in several ways. In this paper, we follow an indirect path that might seem circuitous but allows us to gather further insights on the properties of ADCIGs.

We first demonstrate property (1) by showing that the radial-trace transformations represented by equation 4, and analogously equation 7, are equivalent to a chain of two transformations. The first one is the transformation of the HOCIGs (or VOCIGs) to GOCIGs by a dip-dependent stretching of the offset axis; that is,

$$\widetilde{h_0} = x_h \cos \alpha, \quad \text{or} \quad \widetilde{h_0} = z_h \sin \alpha, \qquad (16)$$

or in the wavenumber domain,

$$k_{h_0} = \frac{k_{x_h}}{\cos \alpha}, \quad \text{or} \quad k_{h_0} = \frac{k_{z_h}}{\sin \alpha}, \qquad (17)$$

where k_{h_0} is the wavenumber associated with $\widetilde{h_0}$, and k_{x_h} and k_{z_h} are the wavenumbers associated with x_h and z_h.

The second is the transformation of HOCIGs to the angle domain according to the relation

$$\tan \gamma = \frac{k_{h_0}}{k_n}, \qquad (18)$$

where k_n is the wavenumber associated with the direction normal to the reflector.

The transformation of HOCIGs to GOCIGs by equations 16 and 17 follows directly from equations 9 and 10. Because the transformation is a dip-dependent stretching of the offset axis, it shifts energy in the (z, x) plane. Appendix A demonstrates that the amount of shift in the (z, x) plane exactly corrects for the image-point shift characterized by equations 11 and 12.

Appendix B demonstrates the geometrical property that for energy dipping at an angle α in the the (z, x) plane, the wavenumber k_n along the normal to the dip is linked to the wavenumbers along (z, x) by

$$k_n = -\frac{k_z}{\cos \alpha} = \frac{k_x}{\sin \alpha}. \qquad (19)$$

Substituting equations 17 and 19 into equation 18, we obtain equations 4 and 7. The graphical interpretation of this ana-

lytical result is immediate. In Figure 3, the transformation to GOCIG (equations 17) moves the imaging point $\mathbf{I_{x_h}}$ (or $\mathbf{I_{z_h}}$) to $\mathbf{I_0}$, and the transformation to the angle domain (equation 18) moves $\mathbf{I_0}$ to $\mathbf{I_\gamma}$. This sequence of two shifts is equivalent to the direct shift from $\mathbf{I_{x_h}}$ (or $\mathbf{I_{z_h}}$) to $\mathbf{I_\gamma}$ caused by the transformation to the angle domain applied to a HOCIG (or VOCIG).

We just demonstrated that the results of the transformation to ADCIGs are independent of which type of offset-domain CIGs we started from (HOCIG, VOCIG, or GOCIG). Consequently, the imaging point $\mathbf{I_\gamma}$ must be common to all kinds of ADCIGs. Furthermore, the image point must lie along each of the normals to the offset directions passing through the respective image points. In particular, it must lie along the normal to the apparent geological dip and at the crossing point of the the vertical line passing through $\mathbf{I_{x_h}}$ and the horizontal line passing through $\mathbf{I_{z_h}}$. Given these constraints, the validity of property (2) (equations 13 and 14) can be easily verified by trigonometry, assuming that the image-point shifts are given by the expressions in equations 9 and 10.

ROBUST COMPUTATION OF ADCIGs IN PRESENCE OF GEOLOGICAL STRUCTURE

Our first application of the CIG kinematic properties analyzed in the previous section is the definition of a robust method to compute high-quality ADCIGs for all events, including steeply dipping and overturned reflections. In the presence of complex geological structure, the computation of neither the conventional HOCIGS nor the new VOCIGs is sufficient to provide complete velocity information because the image is stretched along both the subsurface-offset axes.

According to equation 9, as the geological dip increases, the horizontal-offset axis is stretched. At the limit, when α is equal to $90°$, the relation between the horizontal offset and the geological-dip offset becomes singular. Similarly, VO-CIGs have problems when the geological dip is nearly flat ($\alpha = 0°$) and equation 10 becomes singular. This dip-dependent offset-stretching of the offset-domain CIGs causes artifacts in the corresponding ADCIGs. Furthermore, according to equations 11–12, the image points $\mathbf{I_{x_h}}$ and $\mathbf{I_{z_h}}$ diverge as well in either case.

The fact that relationships 9 and 10 diverge only for isolated dips ($0°, 90°, 180°$, and $270°$) may falsely suggest that problems are limited to rare cases. However, in practice there are two factors that make the computation of ADCIGs in presence of geological dips prone to artifacts:

1) To limit the computational cost, we would like to compute the offset-domain gathers over a range of offsets as narrow as possible. This is particularly true for shot-profile migrations, where the computation of the imaging conditions by equation 2 can add substantially to the computational cost when it is performed over a wide range of subsurface offsets.

2) The attractive properties of the ADCIGs that we demonstrated above, including the elimination of the image-point dispersal, depend on the assumption of locally constant velocity. In particular, velocity is assumed to be constant along the ray segments $\overline{\mathbf{S_{x_h} S_0}}$, $\overline{\mathbf{R_{x_h} R_0}}$, $\overline{\mathbf{S_{z_h} S_0}}$, and $\overline{\mathbf{R_{z_h} R_0}}$ drawn in Figure 2. The longer those segments are, the more likely it is that the constant velocity assumption will be violated sufficiently to cause substantial errors.

These considerations suggest that, in the presence of complex structures, high-quality ADCIGs ought to be computed using the information present in both HOCIGs and VOCIGs. In practice, VOCIGs should be computed in combination with numerical methods that are capable of handling nearly-horizontal propagating events (such as a time-domain propagator or a steep-dips downward-continuation method).

There are two alternative strategies for obtaining a single set of ADCIGs from the information present in HOCIGs and VOCIGs. The first method merges HOCIGs with VOCIGs after they have been transformed to GOCIGs by the application of the offset stretching expressed in equation 16. The merged GOCIGs are then transformed to ADCIGs by applying the radial-trace transformation expressed in equation 18. The second method merges HOCIGs with VOCIGs directly in the angle domain after both have been transformed to ADCIGs by the radial-trace transforms expressed in equations 4 and 7.

The two methods are equivalent if the offset range is infinitely wide, but they may have different artifacts when the offset range is limited. Since the first method merges the images in the offset domain, it can take into account the offset-range limitation more directly and, thus, it has the potential to produce more accurate ADCIGs. However, the second method is more direct and simpler to implement. In both methods, an effective, though approximate, way for taking into account the limited offset ranges is to weight the CIGs as a function of the apparent dips α in the image. A simple weighting scheme is

$$w_{x_h} = \cos^2 \alpha, \quad w_{z_h} = \sin^2 \alpha, \tag{20}$$

where the weights w_{x_h} and w_{z_h} are respectively for the CIGs computed from the HOCIGs and the VOCIGs. These weights have the attractive property that their sum is equal to one for any α. Although the weights are dependent on the geological dip α, their computation is straightforward and accurate in the Fourier domain because they are independent of the spatial coordinates. We used this weighting scheme for all the results shown in this paper.

ADCIGs in the presence of geological structure: A North Sea example

The following marine-data example demonstrates that the application of the robust method for computing ADCIGs presented in this section substantially improves the quality of AD-CIGs in the presence of geological structure. Our examples show migration results of a 2D line extracted from a 3D data set acquired in the North Sea over a salt body with a vertical edge. The data were imaged using a shot-profile reverse time migration, because the reflections from the salt edge had overturned paths.

As predicted by our theory, in the presence of a wide range of reflector dips (e.g., flat sediments and salt edges), both the HOCIGS and the VOCIGs are affected by artifacts. Figure 4 illustrates this problem. It displays orthogonal sections cut through the HOCIG cube (Figure 4a) and the VOCIG cube (Figure 4b). The front faces show the images at zero offset and are the same in the two cubes. The side face of Figure 4a shows the HOCIGs taken at the horizontal location corresponding to the vertical salt edge. We immediately notice that, at the depth

interval corresponding to the salt edge, the image is smeared along the offset axis, which is consistent with the horizontal-offset stretch described by equation 9. On the contrary, the image of the salt edge is well focused in the VOCIG displayed in the top face of Figure 4b, which is consistent with the vertical-offset stretch described by equation 10. However, the flattish reflectors are unfocused in the VOCIG cube, whereas they are well focused in the HOCIG cube. The stretching of the offset axes causes useful information to be lost when significant energy is pushed outside the range of offsets actually computed. In this example, the salt-edge reflection is clearly truncated in the HOCIG cube displayed in Figure 4a, notwithstanding that the image was computed for a fairly wide offset-range (800 m, starting at -375 m and ending at 425 m).

The ADCIGs computed from either the HOCIGs or the VOCIGS have similar problems with artifacts caused by the
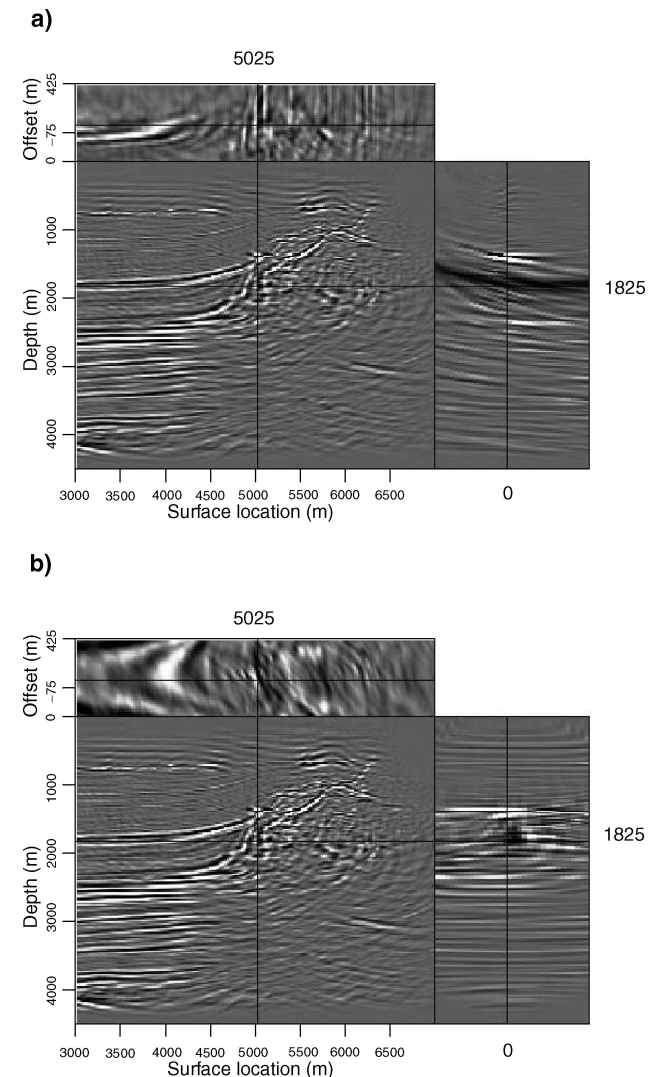

Figure 4. Migrated images of North Sea data set. Orthogonal sections cut through offset-domain CIG cubes: (a) HOCIG cube, (b) VOCIG cube. Notice the artifacts in both cubes. The numbers close to the black lines superimposed onto the orthogonal sections denote the physical coordinates of these sections: $z = 1825$ m, $x = 5025$ m, and $x_h = 0$ m.

wide range of reflectors dips. Figure 5 shows the ADCIG computed from the offset-domain CIGs shown in Figure 4. The salt edge is smeared in the ADCIG computed from HOCIG (side face of Figure 5a), whereas it is fairly well focused in the ADCIG computed from VOCIG (top face of Figure 5b). Conversely, the flattish reflectors are well focused in the AD-CIG computed from HOCIG, whereas they are smeared in the ADCIG computed from VOCIG.

The artifacts are strongly attenuated when the ADCIG cubes shown in Figure 5 are merged according to the simple scheme discussed above, which uses the weights defined in equations (20). Figure 6 shows the ADCIG cube resulting from the merge. The flat moveouts for the salt edge (in the horizontal slice on the top) and the sediment reflections (in the vertical slice on the side) are now clearly visible in the merged ADCIG

cube and confirm the correctness of the migration velocity for the events displayed in the selected ADCIG. To confirm these conclusions we migrated the same data after scaling the slowness function with a constant factor equal to 1.04. Figure 7 shows the ADCIG cubes computed from the HOCIG cube (Figure 7a), and from the VOCIG cube (Figure 7b). When comparing Figure 5 with Figure 7, we notice the 175-m horizontal shift of the salt edge reflection toward the left, caused by the decrease in migration velocity. However, the artifacts related to the salt edge reflection are similar in the two figures, and they similarly obscure the moveout information. On the contrary, the moveout information is ready to be analyzed in the cube displayed in Figure 8, which shows the ADCIG cube resulting from the merge of the ADCIG cubes shown in Figure 7. In particular, both the flattish event above the salt edge (at about 1000-m depth) and the salt edge itself show a typical upward smile in the angle-domain gathers, indicating that the migration velocity was too slow.

ILLUSTRATION OF CIGs KINEMATIC PROPERTIES WITH A SYNTHETIC DATA SET

To verify the results of our geometric analysis of the kinematic properties of CIGs, we modeled and migrated a synthetic data set with a wide range of dips. The reflector has circular shape with radius of 500 m. The center is at 1000-m depth and 3560-m horizontal coordinate. The velocity is constant and equal to 2000 m/s. The data were recorded in 630 shot records. The first shot was located at a surface coordinate of -2000 m, and the shots were spaced 10 m apart. The receiver array was configured with an asymmetric split-spread geometry. The minimum negative offset was constant and equal to -620 m. The maximum offset was 4400 m for all the shots, with the exception of the first 100 shots (from -2000 to -1000 m), where the maximum offset was 5680 m to record all the useful reflections. To avoid boundary artifacts at the top of the model, both sources and receivers were buried 250-m deep. Some of the reflections from the top of the circle were muted out before migration to
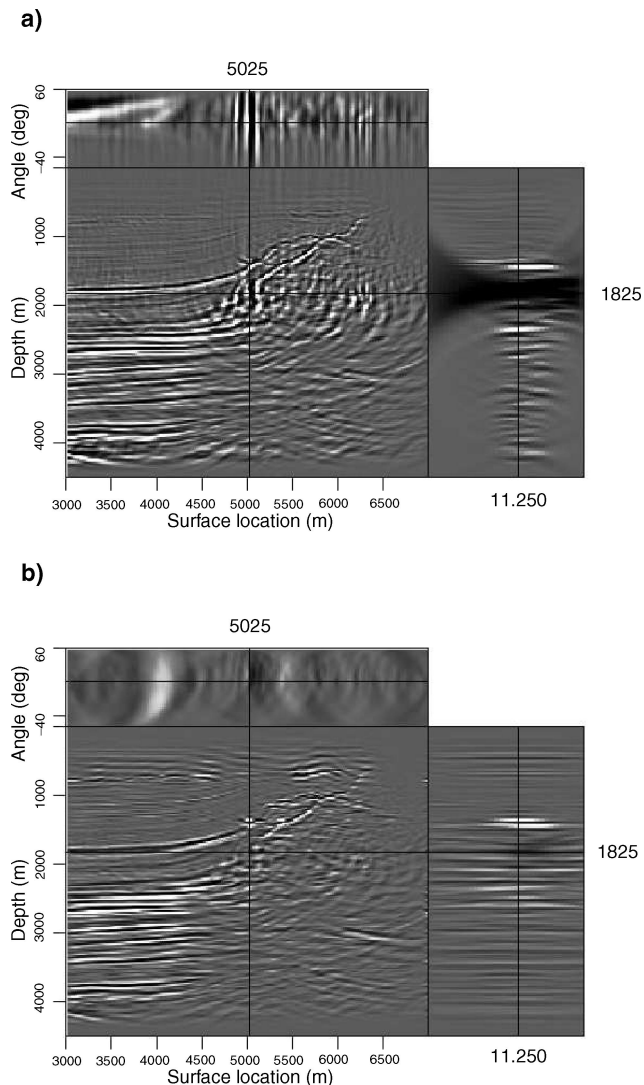
a)

b)

Figure 5. Orthogonal sections cut through ADCIG cubes: (a) ADCIG computed from HOCIG cube, (b) ADCIG computed from VOCIG cube. Notice the artifacts in both cubes that are related to the artifacts visible in the corresponding offset-domain CIG cubes (Figure 4). The coordinates of these sections $z = 1825$ m, $x = 5025$ m, and $\gamma = 11.25°$.
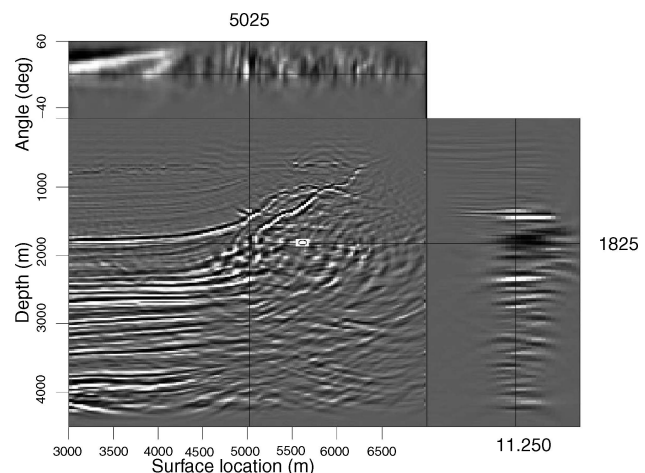

Figure 6. Orthogonal sections cut through the ADCIG cube that was obtained by merging the cubes displayed in Figure 5 using the proposed method. Notice the lack of artifacts compared with Figure 5. The coordinates of these sections are $z = 1825$ m, $x = 5025$ m, and $\gamma = 11.25°$.

avoid migration artifacts caused by spurious correlations with the first arrival of the source wavefield. The whole data set was migrated twice: first using the correct velocity (2000 m/s), and second after scaling the slowness function by a constant factor $\rho = 1.04$ (corresponding to a velocity of 1923 m/s). The ADCIGs shown in this section and the following section were computed by merging the ADCIGs computed from both the HOCIGs and VOCIGs according to the robust algorithm presented in the previous section.

Figure 9a shows the zero-offset section (stack) of the migrated cubes with the correct velocity; Figure 9b shows the zero-offset section obtained with the low velocity. Notice that, despite the large distance between the first shot and the left edge of the circle (about 5000 m), normal incidence reflections

illuminate the target only up to about 70°. As we see in the angle-domain CIGs, the aperture angle coverage shrinks dramatically with increasing reflector dip. On the other hand, real data cases are likely to have a vertical velocity gradient that improves the angle coverage of steeply dipping reflectors.

Transformation of HOCIGs and VOCIGs to GOCIGs

Figure 10 illustrates the differences between HOCIGs and VOCIGs caused by the image-point shift, and it demonstrates that the image-point shift is corrected by the transformation to GOCIGs described in equations 9 and 10.

Figures 10a and 10b show orthogonal sections cut through the offset-domain image cubes in the case of the low-velocity migration. Figure 10a displays the horizontal-offset image cube, whereas Figure 10b displays the vertical-offset image cube. Notice that the offset axis in Figure 10b has been reversed to facilitate its visual correlation with the image cube displayed in Figure 10a. The side faces of the cubes display the CIGs taken at the surface location corresponding to the apparent geological dip of 45°. The events in the two types of CIGs have similar shapes, as expected from the geometric analysis presented in a previous section ($\cos \alpha = \sin \alpha$ when $\alpha = 45°$), but their extents are different. The differences between the two image cubes are more apparent when comparing the front faces, which show the image at a constant offset of 110 m (-110 m in Figure 10b). These differences are due to the differences in image-point shift for the two offset directions (equations 11 and 12).

Figure 10c and 10d show the image cubes of Figures 10a and 10b after the application of the transformations to GOCIG, described in equations 9 and 10, respectively. The two transformed cubes are more similar to each other than the cubes in Figures 10a and 10b are, because both the offset stretching and the image-point shift have been removed. The only significant differences are visible in the front face for the reflections
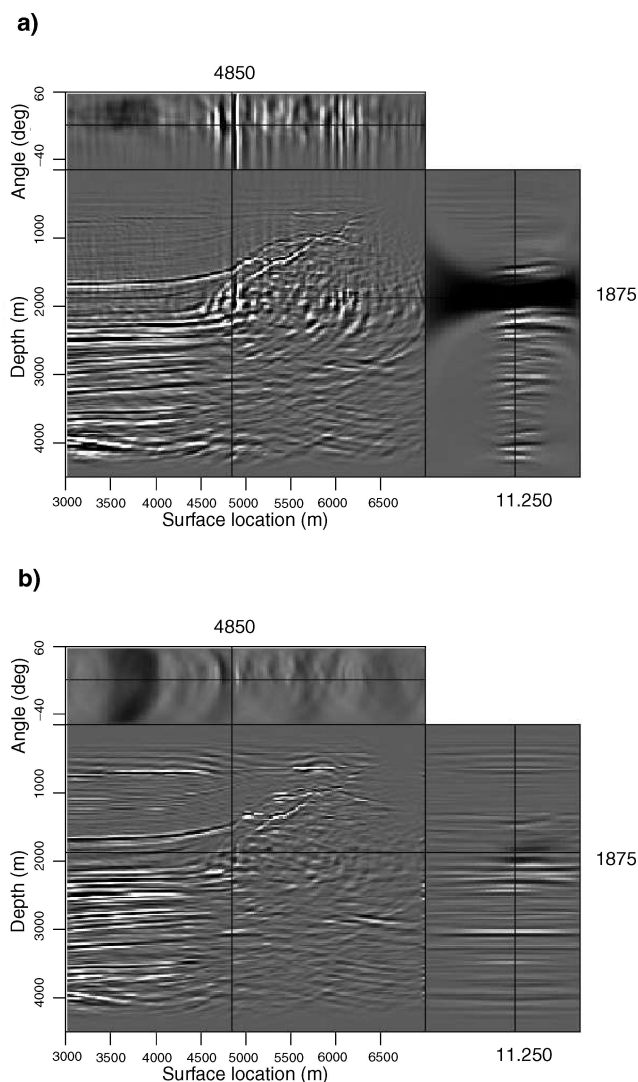

Figure 7. Migrated images of North Sea data set. The migration slowness had been scaled by 1.04 with respect to the migration slowness used for the images shown in Figures 4–6. Orthogonal sections cut through ADCIG cubes: (a) ADCIG computed from HOCIG cube, (b) ADCIG computed from VOCIG cube. Notice that the artifacts obscure the moveout information in both cubes. The coordinates of these sections are $z = 1875$ m, $x = 4850$ m, and $\gamma = 11.25°$.
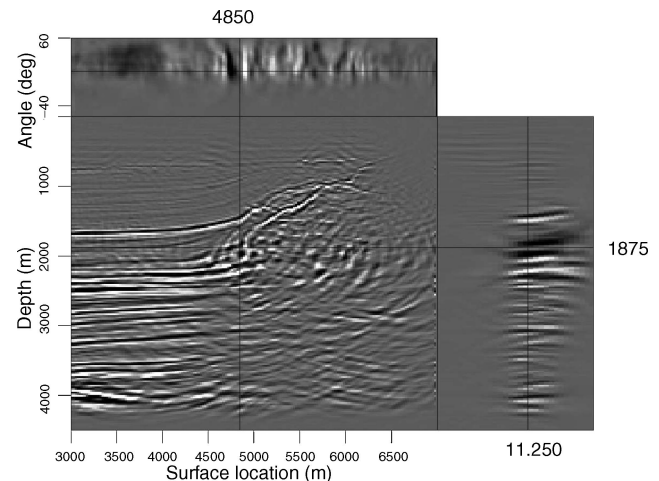

Figure 8. Orthogonal sections cut through the ADCIG cube that was obtained by merging the cubes displayed in Figure 7 using the proposed method. Notice the typical upward smile in the moveouts from both the salt edge and the flattish event above it. The coordinates of these sections are $z = 1875$ m, $x = 4850$ m, and $\gamma = 11.25°$.

corresponding to the top of the circle. These reflections cannot be fully captured within the vertical-offset image cube because the expression in equation 10 diverges as α goes to zero. Similarly, reflections from steeply dipping events are missing from the horizontal-offset image cube because the expression in equation 9 diverges as α goes to $90°$.

Image mispositioning in ADCIGs migrated with wrong velocity

In a previous section, we demonstrated that in an ADCIG cube the imaging point $\mathbf{I}_\gamma$ lies on the line normal to the apparent geological dip and passing through the point where the source and receiver rays cross (Figure 3). This geometric property enabled us to define the analytical relationship between reflector movement and traveltime perturbation expressed in equation 15. This important result is verified by the numerical experiment shown in Figure 11. This figure compares the images of the circular reflector obtained using the low velocity (slowness scaled by $\rho = 1.04$) with the reflector position computed analytically under the assumption that $\mathbf{I}_\gamma$ is indeed the image point in an ADCIG. Because both the true and the migration velocity functions are constant, the migrated reflector location can be computed exactly by a simple "kinematic mi-

gration" of the recorded events. This process takes into account the difference in propagation directions between the "true" events and the "migrated" events caused by the scaling of the velocity function. Appendix C derives the equations used to compute the migrated reflector location as a function of ρ, α_ρ, and γ_ρ.

The images shown in the six panels in Figure 11 correspond to six different apparent aperture angles: (a) $\gamma_\rho = 0°$, (b) $\gamma_\rho = 10°$, (c) $\gamma_\rho = 20°$, (d) $\gamma_\rho = 30°$, (e) $\gamma_\rho = 40°$, (f) $\gamma_\rho = 50°$. The black lines superimposed onto the images are the corresponding reflector locations predicted by the relationships derived in Appendix C. The analytical lines perfectly track the migrated images for all values of γ_ρ. The lines terminate when the corresponding event was not recorded by the data acquisition geometry (described above). The images extend beyond the termination of the analytical lines because the truncation artifacts are affected by the finite-frequency nature of the seismic signal, and thus they are not predicted by the simple kinematic modeling described in Appendix C.

RESIDUAL MOVEOUT IN ADCIGs

The inconsistencies between the migrated images at different aperture angles are the primary source of information for

Figure 9. Images of the synthetic data set obtained with (a) correct velocity, (b) too low velocity ($\rho = 1.04$).
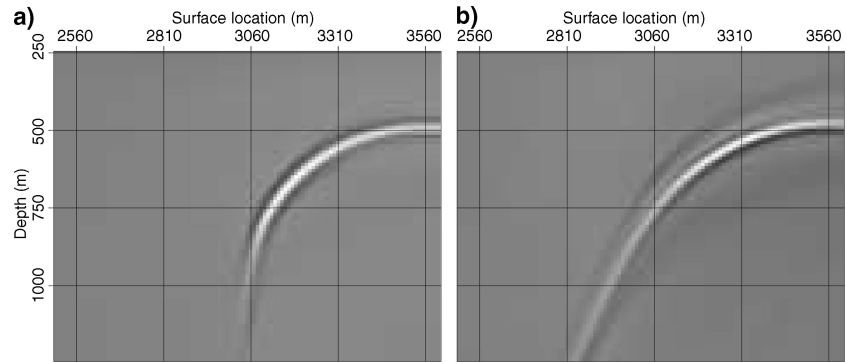

Figure 10. Orthogonal sections cut through offset-domain CIG cubes obtained with too low velocity ($\rho = 1.04$): (a) HOCIG cube, (b) VOCIG cube, (c) GOCIG cube computed from HOCIG cube, (d) GOCIG cube computed from VOCIG cube. Notice the differences between the HOCIG (a) and the VOCIG (b) cubes, and the similarities between the GOCIG cubes (c and d). The coordinates of these sections are $z = 850$ m, $x = 3110$ m, and $x_h = 100$ m.
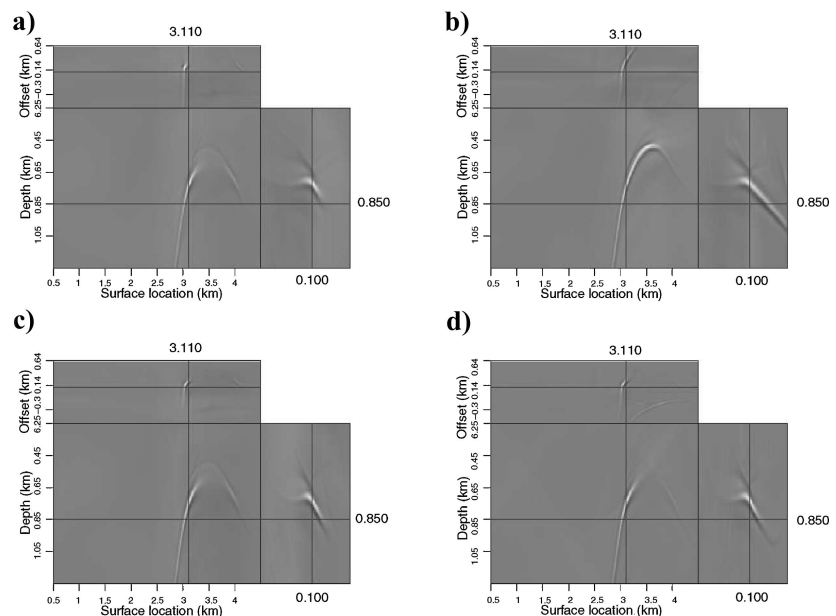
velocity updating during MVA. Figure 11 demonstrates how the reflector mispositioning caused by velocity errors can be exactly predicted by a kinematic migration that assumes the image point to lie on the normal to the apparent geological dip. However, this exact prediction is based on the knowledge of the true velocity model. Of course, this condition is not realistic when we are actually trying to estimate the true velocity model by MVA. In these cases, we first measure the inconsistencies between the migrated images at different aperture angles, and then we "invert" these measures into perturbations of the velocity model.

An effective and robust method for measuring inconsistencies between images is to compute semblance scans as a function of one RMO parameter, and then pick the maxima of the semblance scan. This procedure is most effective when the residual moveout function used for computing the semblance scans closely approximates the true moveouts in the images. In this section, we use the kinematic properties that we derived and illustrated in the previous sections to derive two alternative RMO functions for scanning ADCIGs computed from wavefield-continuation migration.

As discussed above, the exact relationships derived in Appendix C cannot be used because the true velocity function is not known. Thus, we cannot realistically estimate the changes in ray-propagation directions caused by velocity perturbations. However, we can linearize the relations and estimate the reflector movement by assuming that the raypaths are stationary. This assumption is consistent with the typical use of measured RMO functions by MVA procedures. For example, in a tomographic MVA procedure, the velocity is updated by applying a tomographic scheme that "back projects" the image inconsistencies along unperturbed raypaths. Furthermore, the consequences of the errors introduced by neglecting ray bending are significantly reduced by the fact that RMO functions describe the movements of the reflectors relative to the reflector position imaged at normal incidence ($\gamma = 0$), not the absolute movements of the reflectors with respect to the true (unknown) reflector position.

Appendix D derives two expressions for the RMO shift along the normal to the reflector ($\Delta \mathbf{n}_{\mathrm{RMO}}$), under the assumptions of stationary raypaths and constant scaling of the slowness function by a factor ρ. The first expression is (equation D-7)

$$\Delta \mathbf{n}_{\mathrm{RMO}} = \frac{\rho - 1}{\cos \alpha} \frac{\sin^2 \gamma}{(\cos^2 \alpha - \sin^2 \gamma)} z_0 \mathbf{n}, \qquad (21)$$

where z_0 is the depth at normal incidence.

The second RMO function is directly derived from the first by assuming flat reflectors ($\alpha = 0$) (equation D-8):

$$\Delta \mathbf{n}_{\mathrm{RMO}} = (\rho - 1) \tan^2 \gamma z_0 \mathbf{n}. \qquad (22)$$

Albertin et al. (1998) used a similar relationship describing the dependency of RMO with the tangent squared of the opening angle for common-offset Kirchhoff migration.

As expected, in both expressions the RMO shift is null at normal incidence ($\gamma = 0$) and when the migration slowness is equal to the true slowness ($\rho = 1$). According to the first expression (equation 21), the RMO shift increases as a function of the apparent geological dip $|\alpha|$. The intuitive explanation for this behavior is that the specular rays become longer as the apparent geological dip increases, and consequently the effects of the slowness scaling increase. The first expression is more accurate than the second one when the spatial extent of the velocity perturbations is large compared to the raypath length and, consequently, the velocity perturbations are uniformly felt along the entire raypaths. Its use might be advantageous at the beginning of the MVA process when slowness errors are typically large scale. However, it has the disadvantage of depending on the reflector dip α; thus, its application is somewhat more complex.

The second expression is simpler and is not as dependent on the assumption of large-scale velocity perturbations as the first one. Its use might be advantageous for estimating small-scale velocity anomalies at a later stage of the MVA process, when the gross features of the slowness function have been already determined.
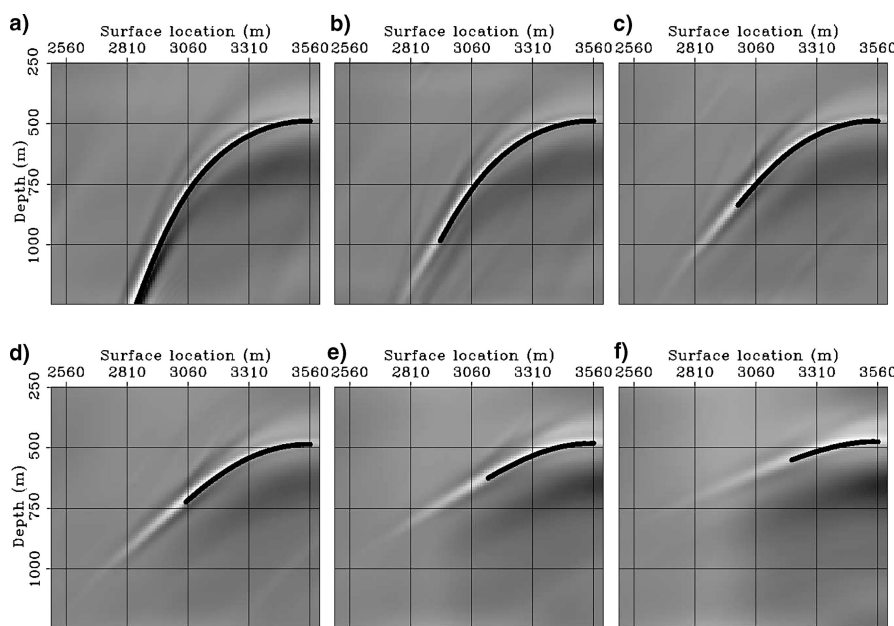

Figure 11. Comparison of the actual images obtained using the low velocity, with the reflector position computed analytically under the assumption that the image point lies on the normal to the apparent geological dip ($\mathbf{I}_\gamma$ in Figure 3). The black lines superimposed onto the images are the reflector locations predicted by the relationships presented in Appendix C. The six panels correspond to six different apparent aperture angles: (a) $\gamma_\rho = 0°$, (b) $\gamma_\rho = 10°$, (c) $\gamma_\rho = 20°$, (d) $\gamma_\rho = 30°$, (e) $\gamma_\rho = 40°$, (f) $\gamma_\rho = 50°$.

The dependency of the RMO function on the geological dip α also highlights the fact that RMO analysis implicitly assumes the existence of coherent reflectors with slowly varying geological dip. When this assumption is not fulfilled, the measurements of RMO from migration results can be misleading.

To test the accuracy of the two RMO functions, we use the migration results of a synthetic data set acquired over a circular reflector. This data set was described in the previous section. Figure 12 illustrates the accuracy of the two RMO functions when predicting the actual RMO in the migrated images obtained with a constant slowness function with $\rho = 1.04$. The four panels show the ADCIGs corresponding to different apparent reflector dip: (a) $\alpha = 0°$, (b) $\alpha = 30°$, (c) $\alpha = 45°$, (d) $\alpha = 60°$. Notice that the vertical axes change across the panels; in each panel, the vertical axis is oriented along the direction normal to the respective apparent geological dip. The solid lines superimposed onto the images are computed using equation 21, whereas the dashed lines are computed using equation 22. As in Figure 11, the images extend beyond the termination of the analytical lines because of the finite-frequency nature of the truncation artifacts.

The migrated images displayed in Figure 12 were computed by setting both the true and the migration slowness function to be constant. Therefore, this case favors the first RMO function (equation 21) because it nearly meets the conditions under which equation 21 is derived in Appendix D. Consequently, the solid lines overlap the migration results for all dip angles. This figure demonstrates that, when the slowness perturbation is sufficiently small (4% in this case), the assumption of stationary raypaths causes only small errors in the predicted RMO.

In contrast, the dashed lines predicted by the second RMO function (equation 22) are an acceptable approximation of the actual RMO function only for small dip angles (up to 30°). For large dip angles, a value of ρ substantially higher than the correct one would be necessary to fit the actual RMO function with equation 22. If this effect of the reflector dip is not properly taken into account, the false indications provided by the inappropriate use of equation 22 can prevent the MVA process from converging.

CONCLUSIONS

We analyze the kinematic properties of ADCIGs in the presence of velocity errors. We prove that in the angle domain the image point lies along the normal to the apparent reflector dip. This geometric property of ADCIGs makes them immune to the image-point dispersal and thus attractive for MVA.

We derive a quantitative relationship between image-point movements and traveltime perturbations caused by velocity errors, and verify its validity with a synthetic-data example. This relationship should be at the basis of velocity-updating methods that exploit the velocity information contained in ADCIGs.

Our analysis leads to the definition of two RMO functions that can be used to measure inconsistencies between migrated images at different aperture angles. The RMO functions describe the relative movements of the imaged reflectors only approximately because they are derived assuming stationary raypaths. However, a synthetic example shows that, when the velocity perturbation is sufficiently small, one of the proposed RMO functions is accurate for a wide range of reflector dips and aperture angles.

The insights gained from our kinematic analysis explain the strong artifacts that affect conventional ADCIGs in presence of steeply dipping reflectors. They also suggest a procedure for overcoming the problem: the computation of VOCIGs followed by the combination of VOCIGs with conventional

Figure 12. ADCIGs for four different apparent reflector dips: (a) $\alpha = 0°$, (b) $\alpha = 30°$, (c) $\alpha = 45°$, (d) $\alpha = 60°$, with $\rho = 1.04$. Superimposed onto the images are the RMO functions computed using equation 21 (solid lines) and using equation 22 (dashed lines). Notice that the vertical axes change across the panels; in each panel, the vertical axis is oriented along the direction normal to the respective apparent geological dip.
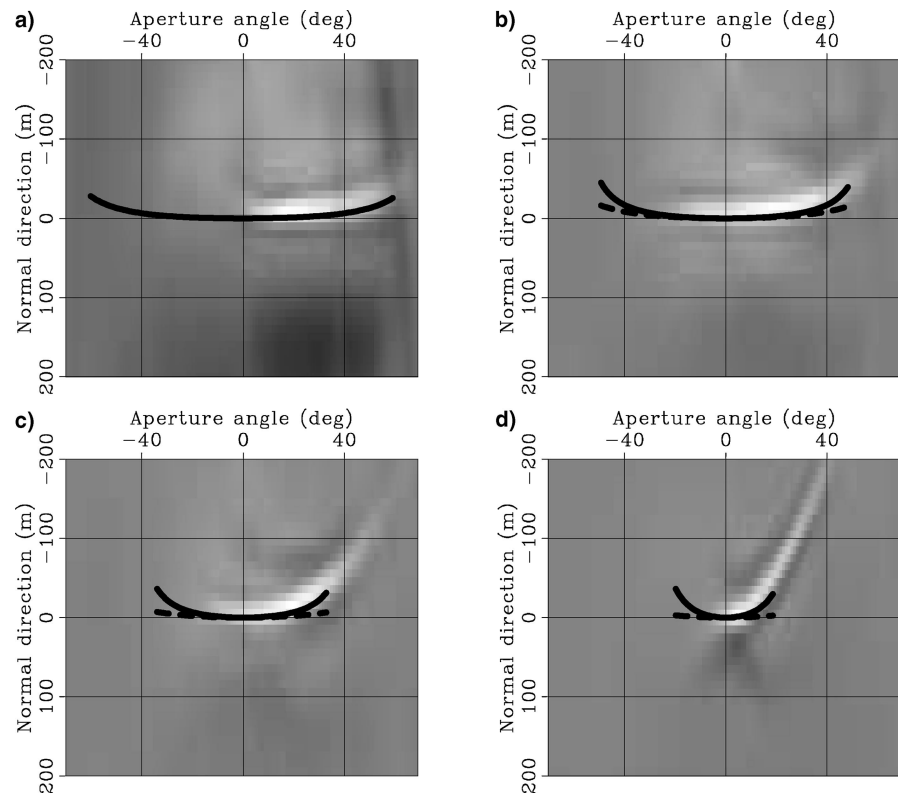
HOCIGs. We propose a simple and robust scheme for combining HOCIGs and VOCIGs. A North Sea data example clearly illustrates both the need for and the advantages of our method for computing ADCIGs in presence of a vertical salt edge.

ACKNOWLEDGMENTS

We thank Guojian Shan for helping in the development of the program that we used to migrate both the synthetic and the real data sets. We also thank Henri Calandra and Total for making the North Sea data set available to the Stanford Exploration Project (SEP). Biondo Biondi would like to acknowledge the financial support of SEP's sponsors.

The final version of this paper has benefited from the comments of the Associate Editor Paul Fowler and two reviewers: Sam Gray and Kees Wapenaar. In particular, Sam Gray's comments motivated us to improve our description of the connection between our ray-theoretical analysis and the wave-theoretical interpretation of ADCIGs. Finally, Bill Schneider, Jr., pointed out to us a mistake in the RMO equation after reading an earlier version of the paper. We are grateful to him for the timely observation and for having spared us the embarrassment of publishing an incorrect equation.

APPENDIX A

PROOF THAT THE TRANSFORMATION TO GOCIG CORRECTS FOR THE IMAGE-POINT SHIFT

This appendix proves that by applying the offset transformations described in equations 9 and 10 we automatically remove the image-point shift characterized by equations 11 and 12. The demonstration for the VOCIG transformation is similar to the one for the HOCIG transformation, and thus we present only the demonstration for the HOCIGs. HOCIGs are transformed into GOCIGs by applying the following change of variables of the offset axis x_h in the vertical wavenumber k_z and horizontal wavenumber k_x domain:

$$x_h = \frac{\widetilde{h_0}}{\cos\alpha} = \text{sign}(\tan\alpha)\,\widetilde{h_0}\sqrt{1+\tan^2\alpha}$$

$$= \text{sign}\left(\frac{k_x}{k_z}\right)\widetilde{h_0}\left(1+\frac{k_x^2}{k_z^2}\right)^{\frac{1}{2}}. \quad\quad (A\text{-}1)$$

For the sake of simplicity, in the rest of the appendix we will drop the sign in front of expression A-1 and consider only the positive values of k_x/k_z.

We want to prove that by applying expression A-1 we also automatically shift the image by

$$\Delta \mathbf{I}_{x_h} \cdot \mathbf{z} = \widetilde{h_0}\tan\gamma\tan\alpha\sin\alpha \quad\quad (A\text{-}2)$$

in the vertical direction and

$$\Delta \mathbf{I}_{x_h} \cdot \mathbf{x} = \widetilde{h_0}\tan\gamma\tan\alpha\cos\alpha \qu\quad (A\text{-}3)$$

in the horizontal direction.

The demonstration is carried out into two steps: (1) we compute the kinematics of the impulse response of transformation A-1 by a stationary-phase approximation of the inverse Fourier transform along k_z and k_x, and (2) we evaluate the dips of the

impulse response, relate them to the angles α and γ, and then demonstrate that relations A-3 and A-2 are satisfied.

Evaluation of the impulse response of the transformation to GOCIGs

The transformation to GOCIG of an image $I_{x_h}(k_z, k_x, x_h)$ is defined as

$$I_0(k_z, k_x, x_h) = \int d\widetilde{h_0} I_0(k_z, k_x, \widetilde{h_0})e^{ik_h\widetilde{h_0}}$$

$$= \int dx_h \left(\frac{d\widetilde{h_0}}{dx_h}\right) I_{x_h}(k_z, k_x, x_h)e^{ik_h x_h\left(1+\frac{k_x^2}{k_z^2}\right)^{\frac{1}{2}}}. \quad\quad (A\text{-}4)$$

The transformation to GOCIG of an impulse located at $(\bar{z}, \bar{x}, \bar{x}_h)$ is thus (after inverse Fourier transforms)

$$\widetilde{\text{Imp}}(z, x, \widetilde{h_0}) = \int dk_h \int dx_h \int dk_x \int dk_z \left(\frac{d\widetilde{h_0}}{dx_h}\right)$$

$$\times e^{i\left\{k_h\left[\bar{x}_h\left(1+\frac{k_x^2}{k_z^2}\right)^{-\frac{1}{2}}-\widetilde{h_0}\right]+k_z(\bar{z}-z)+k_x(\bar{x}-x)\right\}}. \qu\quad (A\text{-}5)$$

We now approximate by stationary phase the inner double integral. The phase of this integral is

$$\Phi \equiv k_h\left[\bar{x}_h\left(1+\frac{k_x^2}{k_z^2}\right)^{-\frac{1}{2}}-\widetilde{h_0}\right]+k_z(\bar{z}-z)+k_x(\bar{x}-x). \ququad (A\text{-}6)$$

The stationary path is defined by the solutions of the following system of equations:

$$\frac{\partial\Phi}{\partial k_z} = k_h\bar{x}_h\frac{k_x^2}{k_z^3}\left(1+\frac{k_x^2}{k_z^2}\right)^{-\frac{3}{2}}+(\bar{z}-z) = 0, \ququad (A\text{-}7)$$

$$\frac{\partial\Phi}{\partial k_x} = -k_h\bar{x}_h\frac{k_x}{k_z^2}\left(1+\frac{k_x^2}{k_z^2}\right)^{-\frac{3}{2}}+(\bar{x}-x) = 0, \quad (A\text{-}8)$$

By moving both $(\bar{z}-z)$ and $(\bar{x}-x)$ to the right of equations A-7 and A-8, and then dividing equation A-7 by equation A-8, we obtain the following relationship between $(\bar{z}-z)$ and $(\bar{x}-x)$:

$$\frac{\bar{z}-z}{\bar{x}-x} = -\frac{k_x}{k_z}. \ququad (A\text{-}9)$$

Furthermore, by multiplying equation A-7 by k_z and equation A-8 by k_x, and then substituting them appropriately in the phase function A-6, we can evaluate the phase function along the stationary path as follows:

$$\Phi_{\text{stat}} = k_h\left[\bar{x}_h\left(1+\frac{k_x^2}{k_z^2}\right)^{-\frac{1}{2}}-\widetilde{h_0}\right], \ququad (A\text{-}10)$$

which becomes, by substituting equation A-9,

$$\Phi_{\text{stat}} = k_h\left\{\bar{x}_h\left[1+\frac{(\bar{z}-z)^2}{(\bar{x}-x)^2}\right]^{-\frac{1}{2}}-\widetilde{h_0}\right\}. \ququad (A\text{-}11)$$

By substituting expression A-11 in equation A-5, we can evaluate the kinematics of the impulse response as follows:

$$\widetilde{h_0} = x_h \left[1 + \frac{(\bar{z} - z)^2}{(\bar{x} - x)^2} \right]^{-\frac{1}{2}}. \quad (A\text{-}12)$$

Evaluation of the image shift as a function of α ad γ

The final step is to take the derivative of the impulse response of equation A-12 and use the relationships of these derivatives with $\tan\alpha$ and $\tan\gamma$:

$$\frac{\partial z}{\partial x} = \tan\alpha = -\sqrt{\frac{x_h^2}{\widetilde{h_0}^2} - 1}, \quad (A\text{-}13)$$

$$-\frac{\partial z}{\partial x_h} = \tan\gamma = -(\bar{x} - x)\frac{\frac{x_h}{\widetilde{h_0}}}{\sqrt{\frac{x_h^2}{\widetilde{h_0}^2} - 1}} = -(\bar{z} - z)\frac{\frac{x_h}{\widetilde{h_0}}}{\frac{x_h^2}{\widetilde{h_0}^2} - 1}. \quad (A\text{-}14)$$

By substituting equations A-13 and A-14 into

$$\Delta \mathbf{I}_{x_h} \cdot \mathbf{z} = \bar{z} - z = \widetilde{h_0} \tan\gamma \tan\alpha \sin\alpha, \quad (A\text{-}15)$$

$$\Delta \mathbf{I}_{x_h} \cdot \mathbf{x} = \bar{x} - x = \widetilde{h_0} \tan\gamma \tan\alpha \cos\alpha, \quad (A\text{-}16)$$

and after some algebraic manipulation, we prove the thesis.

APPENDIX B

RELATIONSHIP BETWEEN WAVENUMBERS AND GEOLOGICAL DIPS

This appendix demonstrates equations 19 in the main text: that for energy dipping at an angle α in the (z, x) plane, the wavenumber k_n along the normal to the dip is linked to the wavenumbers k_z and k_x by

$$k_n = -\frac{k_z}{\cos\alpha} = \frac{k_x}{\sin\alpha}. \quad (B\text{-}1)$$

For energy dipping at an angle α, the wavenumbers satisfy the well-known relationship

$$\tan\alpha = -\frac{k_x}{k_z}, \quad (B\text{-}2)$$

where the negative sign is determined by the conventions defined in Figure 1. The wavenumber k_n is related to k_x and k_z by the axes rotation

$$k_n = -k_z \cos\alpha + k_x \sin\alpha. \quad (B\text{-}3)$$

Substituting equation B-2 into equation B-3, we obtain

$$k_n = \frac{k_z}{\cos\alpha}(-\cos^2\alpha - \tan\alpha \cos\alpha \sin\alpha)$$

$$= -\frac{k_z}{\cos\alpha}(\cos^2\alpha + \sin^2\alpha) = -\frac{k_z}{\cos\alpha}, \quad (B\text{-}4)$$

or

$$k_n = \frac{k_x}{\sin\alpha}(\cot\alpha \sin\alpha \cos\alpha + \sin^2\alpha)$$

$$= \frac{k_x}{\sin\alpha}(\cos^2\alpha + \sin^2\alpha) = \frac{k_x}{\sin\alpha}. \quad (B\text{-}5)$$

APPENDIX C

KINEMATIC MIGRATION OF REFLECTIONS FROM A CIRCLE

In this appendix, we derive the equations for the "kinematic migration" of the reflections from a sphere as a function of the ratio ρ between the true constant slowness S and the migration slowness $S_\rho = \rho S$. For a given ρ, we want to find the coordinates (z_γ, x_γ) of the imaging point $\mathbf{I}_\gamma$ as a function of the apparent geological dip α_ρ and the apparent aperture angle γ_ρ. Central to our derivation is the assumption that the imaging point $\mathbf{I}_\gamma$ lies on the normal to the apparent reflector dip passing through $\bar{\mathbf{I}}$, as represented in Figure 3.

The first step is to establish the relationships between the true α and γ and the apparent α_ρ and γ_ρ. This can be done through the relationships between the propagation directions of the source/receiver rays (respectively marked as the angles β_s and β_r in Figure 1) and the event time dips, which are independent on the migration slowness. The true β_s and β_r can be thus estimated as

$$\beta_s = \arcsin(\rho \sin\beta_{s\rho}) = \arcsin[\rho \sin(\alpha_\rho - \gamma_\rho)], \quad (C\text{-}1)$$

$$\beta_r = \arcsin(\rho \sin\beta_{r\rho}) = \arcsin[\rho \sin(\alpha_\rho + \gamma_\rho)]. \quad (C\text{-}2)$$

Then, the true α and γ are

$$\alpha = \frac{\beta_s + \beta_r}{2} \quad \text{and} \quad \gamma = \frac{\beta_r - \beta_s}{2}. \quad (C\text{-}3)$$

Next step is to take advantage of the fact that the reflector is a sphere and, thus, that the coordinates $(\hat{z}, \hat{x})$ of the true reflection point are uniquely identified by the dip angle α:

$$\hat{z} = (z_c - R\cos\alpha) \quad \text{and} \quad \hat{x} = (x_c + R\sin\alpha), \quad (C\text{-}4)$$

where (z_c, x_c) are the coordinates of the center of the sphere and R is its radius.

The midpoint, offset, and traveltime of the event can be found by applying simple trigonometry (see Sava and Fomel 2003) as follows:

$$x_{h\,\text{surf}} = \frac{\sin\gamma \cos\gamma}{\cos^2\alpha - \sin^2\gamma}\hat{z}, \quad (C\text{-}5)$$

$$x_{m\,\text{surf}} = \hat{x} + \frac{\sin\alpha \cos\alpha}{\cos^2\alpha - \sin^2\gamma}\hat{z}, \quad (C\text{-}6)$$

$$t_D = 2S\frac{\cos\alpha \cos\gamma}{\cos^2\alpha - \sin^2\gamma}\hat{z}. \quad (C\text{-}7)$$

The coordinates $(\bar{z}, \bar{x})$, of the point $\bar{\mathbf{I}}$, where the source and the receiver rays cross, are

$$\bar{z} = x_{h\,\text{surf}}\frac{\cos^2\alpha_\rho - \sin^2\gamma_\rho}{\sin\gamma_\rho \cos\gamma_\rho}, \quad (C\text{-}8)$$

$$\bar{x} = x_{m\,\text{surf}} - \frac{\sin\alpha_\rho \cos\alpha_\rho}{\cos^2\alpha_\rho - \sin^2\gamma_\rho}\bar{z}$$

$$= x_{m\,\text{surf}} - \frac{\sin\alpha_\rho \cos\alpha_\rho}{\cos^2\alpha_\rho - \sin^2\gamma_\rho}\frac{\cos^2\alpha_\rho - \sin^2\gamma_\rho}{\sin\gamma_\rho \cos\gamma_\rho}x_{h\,\text{surf}}$$

$$= x_{m\,\text{surf}} - \frac{\sin\alpha_\rho \cos\alpha_\rho}{\sin\gamma_\rho \cos\gamma_\rho}x_{h\,\text{surf}}, \quad (C\text{-}9)$$

and the corresponding traveltime t_{D_ρ} is

$$t_{D_\rho} = 2\rho S \frac{\cos \alpha_\rho \cos \gamma_\rho}{\cos^2 \alpha_\rho - \sin^2 \gamma_\rho} \bar{z}. \qquad \text{(C-10)}$$

Once we have the traveltimes t_D and t_{D_ρ}, the normal shift $\Delta \mathbf{n}_{\text{tot}}$ can be easily evaluated by applying equation 15 (where the background velocity is S_ρ and the aperture angle is γ_ρ), which yields

$$\Delta \mathbf{n}_{\text{tot}} = \frac{(t_{D_\rho} - t_D)}{2\rho S \cos \gamma_\rho} \mathbf{n}. \qquad \text{(C-11)}$$

We used equation C-11, together with equations C-8 and C-9, to compute the lines superimposed onto the images in Figure 11.

APPENDIX D

RESIDUAL MOVEOUT IN ANGLE-DOMAIN COMMON IMAGE GATHERS

In this appendix, we derive the expression for the RMO function to be applied to ADCIGs computed by wavefield continuation. The derivation follows the derivation presented in Appendix C. The main difference is that in this appendix we assume the rays to be stationary. In other words, we assume that the apparent dip angle α_ρ and aperture angle γ_ρ are the same as the true angles α and γ. This assumption also implies that the (unknown) true reflector coordinates $(\hat{z}, \hat{x})$ coincide with the coordinates $(\bar{z}, \bar{x})$ of the point $\bar{\mathbf{I}}$ where the source and the receiver ray cross.

Given these assumptions, the total traveltime through the perturbed slowness function S_ρ is given by

$$t_{D_\rho} = 2\rho S \frac{\cos \alpha \cos \gamma}{\cos^2 \alpha - \sin^2 \gamma} \bar{z}, \qquad \text{(D-1)}$$

which is different from the corresponding equation in Appendix C (equation C-10). The difference in traveltimes $(t_{D_\rho} - t_D)$, where t_D is given by equation equation C-7, is thus a linear function of the difference in slownesses $[(\rho - 1)S]$; that is,

$$t_{D_\rho} - t_D = 2(\rho - 1) S \frac{\cos \alpha \cos \gamma}{\cos^2 \alpha - \sin^2 \gamma} \bar{z}. \qquad \text{(D-2)}$$

As in Appendix C, the normal shift $\Delta \mathbf{n}_{\text{tot}}$ can be evaluated by applying equation 15 (where the background velocity is S_ρ and the aperture angle is γ), which yields

$$\Delta \mathbf{n}_{\text{tot}} = \frac{\rho - 1}{\rho} \frac{\cos \alpha}{\cos^2 \alpha - \sin^2 \gamma} \bar{z} \mathbf{n}. \qquad \text{(D-3)}$$

The RMO function ($\Delta \mathbf{n}_{\text{RMO}}$) describes the relative movement of the image point at any γ with respect to the image point for the normal-incidence event ($\gamma = 0$). From equation D-3, it follows that the RMO function is

$$\Delta \mathbf{n}_{\text{RMO}} = \Delta \mathbf{n}_{\text{tot}}(\gamma) - \Delta \mathbf{n}_{\text{tot}}(\gamma = 0)$$
$$= \frac{\rho - 1}{\rho} \left[\frac{\cos \alpha}{\cos^2 \alpha - \sin^2 \gamma} - \frac{1}{\cos \alpha} \right] \bar{z} \mathbf{n}$$
$$= \frac{\rho - 1}{\rho} \frac{\sin^2 \gamma}{(\cos^2 \alpha - \sin^2 \gamma) \cos \alpha} \bar{z} \mathbf{n}. \qquad \text{(D-4)}$$

The true depth $\bar{z}$ is not known, but at normal incidence it can be estimated as a function of the migrated depth z_0 by inverting the

following relationship (derived from equation D-3 with $\gamma = 0$):

$$z_0 = \frac{\bar{z}}{\rho}, \qquad \text{(D-5)}$$

as

$$\bar{z} = \rho z_0. \qquad \text{(D-6)}$$

Substituting relation D-6 in equation D-4, we obtain

$$\Delta \mathbf{n}_{\text{RMO}} = \frac{\rho - 1}{\cos \alpha} \frac{\sin^2 \gamma}{(\cos^2 \alpha - \sin^2 \gamma)} z_0 \mathbf{n}, \qquad \text{(D-7)}$$

which for flat reflectors ($\alpha = 0$) simplifies to

$$\Delta \mathbf{n}_{\text{RMO}} = (\rho - 1) \tan^2 \gamma \, z_0 \mathbf{n}. \qquad \text{(D-8)}$$

In Figure 12, the solid lines superimposed into the images are computed using equation D-7, whereas the dashed lines are computed using equation D-8.

REFERENCES

Albertin, U., J. Kapoor, and W. Chang, 1998, Velocity resolution and salt boundary placement in subsalt imaging: Part 1: 68th Annual International Meeting, SEG, Expanded Abstracts, 1297–1300.

Baysal, E., D. D. Kosloff, and J. W. C. Sherwood, 1983, Reverse time migration: Geophysics, **48**, 1514–1524.

Biondi, B., 2003, Equivalence of source-receiver migration and shot-profile migration: Geophysics, **68**, 1340–1347.

Biondi, B., and P. Sava, 1999, Wave-equation migration velocity analysis, 69th Annual International Meeting, SEG, Expanded Abstracts, 1723–1726.

Biondi, B., and G. Shan, 2002, Prestack imaging of overturned reflections by reverse time migration: 72nd Annual International Meeting, SEG, Expanded Abstracts, 1284–1287.

Biondi, B., T. Tisserant, and W. Symes, 2003, Wavefield-continuation angle-domain common-image gathers for migration velocity analysis: 73rd Annual International Meeting, SEG, 2104–2107.

Brandsberg-Dahl, S., M. de Hoop, and B. Ursin, 1999, Velocity analysis in the common scattering-angle/azimuth domain: 69th Annual International Meeting, SEG, Expanded Abstracts, 1715–1718.

———— 2003, Focusing in dip and AVA compensation on scattering-angle/azimuth common image gathers: Geophysics, **68**, 232–254.

Clapp, R., and B. Biondi, 2000, Tau domain migration velocity analysis using angle CRP gathers and geologic constraints: 70th Annual International Meeting, SEG, 926–929.

de Bruin, C. G. M., C. P. A. Wapenaar, and A. J. Berkhout, 1990 Angle-dependent reflectivity by means of prestack migration: Geophysics, **55**, 1223–1234.

de Bruin, C., 1992, Linear AVO inversion by prestack depth migration: Delft University.

de Hoop, M., J. Le Rousseau, and B. Biondi, 2004, Symplectic structure of wave-equation imaging: A path-integral approach based on the double-square-root equation: Journal of Geophysical Research, in press.

Etgen, J., 1986, Prestack reverse time migration of shot profiles: SEP–**50**, 151–170. Available at http://sep.stanford.edu/research/reports.

Etgen, J., 1990, Residual prestack migration and interval velocity estimation: Ph.D. dissertation, Stanford University.

Liu, W., A. Popovici, D. Bevc, and B. Biondi, 2001, 3-D migration velocity analysis for common image gathers in the reflection angle domain: 69th Annual International Meeting, SEG, Expanded Abstracts, 885–888.

Meng, Z., and N. Bleistein, 2001, On velocity/depth ambiguity in 3-D migration velocity analysis: Geophysics, **66**, 256–260.

Mosher, C. C., D. J. Foster, and S. Hassanzadeh, 1997, Common angle imaging with offset plane waves: 67th Annual International Meeting, SEG, Expanded Abstracts, 1379–1382.

Mosher, C., S. Jin, and D. Foster, 2001, Migration velocity analysis using common angle image gathers: 71th Annual International Meeting, SEG, 889–892.

Prucha, M., B. Biondi, and W. Symes, 1999, Angle-domain common-image gathers by wave-equation migration: 69th Annual International Meeting, SEG, Expanded Abstracts, 824–827.

Rickett, J., and P. Sava, 2002, Offset and angle-domain common image-point gathers for shot-profile migration: Geophysics, **67**, 883–889.

Sava, P., B. Biondi, and S. Fomel, 2001, Amplitude-preserved common image gathers by wave-equation migration: 71st Annual International Meeting, SEG, Expanded Abstracts, 296–299.

Sava, P., and S. Fomel, 2003, Angle-domain common-image gathers by wavefield continuation methods: Geophysics, **68**, 1065–1074.

Schultz, P. S., and J. F. Claerbout, 1978, Velocity estimation and downward-continuation by wavefront synthesis: Geophysics, **43**, no. 4, 691–714.

Stolk, C. C., and W. W. Symes, 2004, Kinematic artifacts in prestack depth migration: Geophysics, **69**, 562–575.

Stork, C., 1992, Reflection tomography in the postmigrated domain: Geophysics, **57**, 680–692.

Stork, C., P. Kitchenside, D. Yingst, U. Albertin, C. Kostov, B. Wilson, D. Watts, J. Kapoor, and G. Brown, 2002, Comparison between angle and offset gathers from wave equation migration and Kirchhoff migration: 72nd Annual International Meeting, SEG, Expanded Abstracts, 1200–1203.

Wapenaar, C. P. A., and A. J. Berkhout, 1987, Full prestack versus shot record migration: 69th Annual International Meeting, SEG, Expanded Abstracts, Session:S15.7.

Wapenaar, K., A. Van Wijngaarden, W. van Geloven, and T. van der Leiji, 1999, Apparent AVA effects of fine layering: Geophysics, **64**, 1939–1948.

Whitmore, N. D., 1983, Iterative depth migration by backward time propagation: 53rd Annual International Meeting, SEG, Expanded Abstracts, Session S10.1.

Xie, X. B., and R. S. Wu, 2002, Extracting angle domain information from migrated wavefield: 72th Annual International Meeting, SEG, 1360–1363.

Xu, S., H. Chauris, G. Lambaré, and M. S. Noble, 2001, Common-angle migration: A strategy for imaging complex media: Geophysics, **66**, 1877–1894.